ORNL/SPR-2020/1742

# Demonstrate Embedding of Sensors in a Relevant Microreactor Component


Christian M. Petrie
Nora Dianne B. Ezell

**November 6, 2020**

**Approved for public release.
Distribution is unlimited.**

OAK RIDGE NATIONAL LABORATORY
MANAGED BY UT-BATTELLE FOR THE US DEPARTMENT OF ENERGY

**ORNL/SPR-2020/1742**

Reactor and Nuclear Systems Division

# DEMONSTRATE EMBEDDING OF SENSORS IN A RELEVANT MICROREACTOR COMPONENT

Christian M. Petrie
Nora Dianne B. Ezell

Date Published: November 6, 2020

**Milestone #: M3AT-21OR0804053**

Prepared by
OAK RIDGE NATIONAL LABORATORY
Oak Ridge, TN 37831-6283
managed by
UT-BATTELLE, LLC
for the
US DEPARTMENT OF ENERGY
under contract DE-AC05-00OR22725

**CONTENTS**

## LIST OF FIGURES

## ACRONYMS AND ABBREVIATIONS

| | |
|---|---|
| BN | boron nitride |
| CH | cartridge heater |
| CNC | computer numerical control |
| DOE | US Department of Energy |
| TC | thermocouple |
| TCR | Transformational Challenge Reactor |
| HP | heat pipe |
| ID | inner diameter |
| INL | Idaho National Laboratory |
| LANL | Los Alamos National Laboratory |
| LDRD | Laboratory Directed Research and Development |
| MAGNET | Microreactor Agile Non-nuclear Testbed |
| OD | outer diameter |
| ORNL | Oak Ridge National Laboratory |
| UAM | ultrasonic additive manufacturing |
| UTS | ultimate tensile stress |

## ACKNOWLEDGMENTS

This research was sponsored by the Microreactor Research, Development, and Deployment Program of the US Department of Energy (DOE) Office of Nuclear Energy. The report was authored by UT-Battelle under Contract No. DE-AC05-00OR22725 with DOE. Dan King, Adam Hehr, and Mark Norfolk (Fabrisonic, LLC) performed the sensor embedding. Adrian Schrell and Daniel Sweeney (Oak Ridge National Laboratory, ORNL) performed the fiber-optic measurements before and after embedding, respectively. Holly Trellue (Los Alamos National Laboratory) provided the 3D-printed hex block for sensor embedding.

## SUMMARY

This report describes the first successful embedding of sensors in stainless steel pipe specimens and a miniature hex block to support structural health monitoring of microreactor components during electrically heated testing in non-nuclear testbed facilities. Sensors were embedded with an ultrasonic additive manufacturing process that uses a combination of downward pressure and an ultrasonic scrubbing motion to bond stainless steel foils to underlying materials. After placing sensors within cavities that have been machined to the size of the sensors, the ultrasonic bonding process fills the gaps around the sensors and embeds them within the part. Both Type K thermocouples and spatially distributed fiber-optic strain sensors were successfully embedded within two pipe specimens and a miniature hex block. After the fiber-optic sensors were embedded, they were interrogated and found to have minimal signal attenuation within the embedded region—a significant improvement compared to previous trials. This is likely because of the low-bend-loss fiber that was used, which greatly reduces microbending losses that occur after the embedding process. In addition to showing minimal signal attention, the fibers also showed adequate compressive strain, which is a strong indication that the sensors are physically embedded in the parts as opposed to simply being loosely contained inside the machined cavities. The embedded fibers were able to capture the strain induced in one of the pipe specimens while the pipe was actively heated with a moving heat source.

Finite element simulations were performed to determine the expected temperatures and strains that the embedded sensors would need to measure during non-nuclear thermal testing. Models were developed to simulate the temperatures and stresses within a monolithic steel hex block that is internally heated using six cartridge heaters (CHs) and cooled using a single heat pipe. The modeling results indicated that the single heat pipe test will result in small compressive strains at the outer surface of the hex block where the sensors are embedded. While these strains are measurable using the embedded fiber-optic strain sensors, the limiting tensile strains occur at the cooler inner surface of the hex block where the heat is transferred to the heat pipe. This surface cannot be accessed using embedded sensors or non-contact techniques. Nevertheless, the embedded fiber-optic strain sensors are capable of resolving the small compressive strains at the outer surface if they can survive differential thermal expansion between the hex block and the fibers at the anticipated high operating temperatures. The simulations also show the importance of using thermally conductive materials such as boron nitride (BN) to fill the gaps surrounding the heat pipe and the cartridge heaters (CHs) to limit the maximum temperatures, temperature gradients, and resulting thermal stresses. Without surrounding the heat pipe with BN, the structural simulations predict stresses that exceed the ultimate tensile strength of the hex block over the range of expected heater power levels. The power level and associated heat flux to the heat pipe at which the hex block is calculated to fail depends on whether the CHs are surrounded by helium or BN. Furthermore, without surrounding the heat pipe with BN, each CH can only be operated at a maximum power of ~100 W (79 kW/m$^2$ heat flux to the heat pipe) before the temperature limits of the cartridge are exceeded, even when the CHs are surrounded by BN. If BN is used to surround both the heat pipe and the CHs, the simulations predict that the hex block will not fail and the predicted temperatures and strains can be measured using the embedded sensors.

# 1. INTRODUCTION

The DOE Office of Nuclear Energy Microreactor program supports early-stage generic research and technology development for microreactor systems for private industry and potential defense applications. The program's Technology Maturation technical area is focused on advancing the technology readiness of instrumentation and sensors for improved non-nuclear testing of microreactor components and systems, as well as improved microreactor health monitoring during nuclear system operation. However, the transition to smaller, more compact microreactors has its own challenges, particularly for instrumentation and sensor deployment.

The compact, largely factory-assembled microreactor cores provide limited space for in-core instrumentation. Because microreactors are often designed for mobile applications, integrating instrumentation into the factory-assembled cores would reduce the need for onsite routing and installation of ex-core instrumentation. This can present challenges when identifying sensors with a small footprint that can survive the harsh in-core environment, particularly for advanced microreactor concepts with higher operating temperatures and longer refueling cycles compared to those of traditional light water reactors. In addition, the greatly reduced power output of microreactors concepts requires reductions in operation and maintenance costs to be economically viable. One way to accomplish this is by increasing online health monitoring capabilities and ultimately moving towards autonomous control to reduce staffing and reliance on human intervention. Finally, the transition to smaller cores generally results in higher neutron leakage and more significant spatial variations in temperature and neutron flux. This presents challenges not only for monitoring and controlling the reactor, but also for the materials that may be affected by differential thermal expansion or radiation-induced dimensional changes resulting from the temperature and flux gradients. This is especially true for monolithic cores such as heat pipe (HP)-based reactors. The ability to monitor the structural health of these in-core components during nuclear operation or out-of-pile thermal testing can provide invaluable data for validation of thermomechanical models supporting microreactor design, licensing, and operation.

This report describes the progress made toward embedding sensors within relevant microreactor structural components to ultimately improve health monitoring capabilities during nuclear and non-nuclear testing. Similar work is being performed to embed sensors in ceramic structures under the Transformational Challenge Reactor (TCR) Program [1]. The present work leverages additive manufacturing technologies that were initially developed using Laboratory Directed Research and Development (LDRD) funding from Oak Ridge National Laboratory (ORNL) [2-5]. The work described herein is a step towards extending ultrasonic additive manufacturing (UAM) technology to embed sensors within more complex metal components relevant to microreactors. This report summarizes the UAM technology, the sensor embedding process, the sensors that were selected for the first embedded sensor demonstration, and the initial results obtained after embedding sensors in stainless steel pipes and a 7-hole additively manufactured hex block, which is similar to what will be tested in future experiments in the Microreactor Agile Non-nuclear Testbed (MAGNET) at Idaho National Laboratory (INL). Finally, analyses are being performed to predict the response of the embedded sensors during non-nuclear thermal testing of a single HP.

# 2. METHODS

## 2.1 ULTRASONIC ADDITIVE MANUFACTURING

UAM is a solid-state welding process that relies on the combination of downward pressure and lateral ultrasonic vibrations to bond metal foils to an underlying substrate or baseplate [6, 7]. The process is illustrated schematically in Figure 1. Ultrasonic welding involves a textured sonotrode and an integrated computer numerical control (CNC) mill, providing both additive and subtractive operations using the same machine. The starting baseplate material can be any wrought material, or it can be manufactured using an additive process. The top surface of the baseplate is typically faced using a finishing mill pass to ensure that the substrate is flat and smooth. A single foil sheet is then placed on the substrate. The sonotrode traverses along the length of the foil while simultaneously applying downward pressure and an ultrasonic scrubbing motion. This causes localized yielding of surface asperities, breakdown of surface oxide layers, and cold welding of the foil to the baseplate. A wide range of foil/baseplate materials can be welded, including aluminum alloys [8], copper [9], nickel alloys [3], and steels [10].

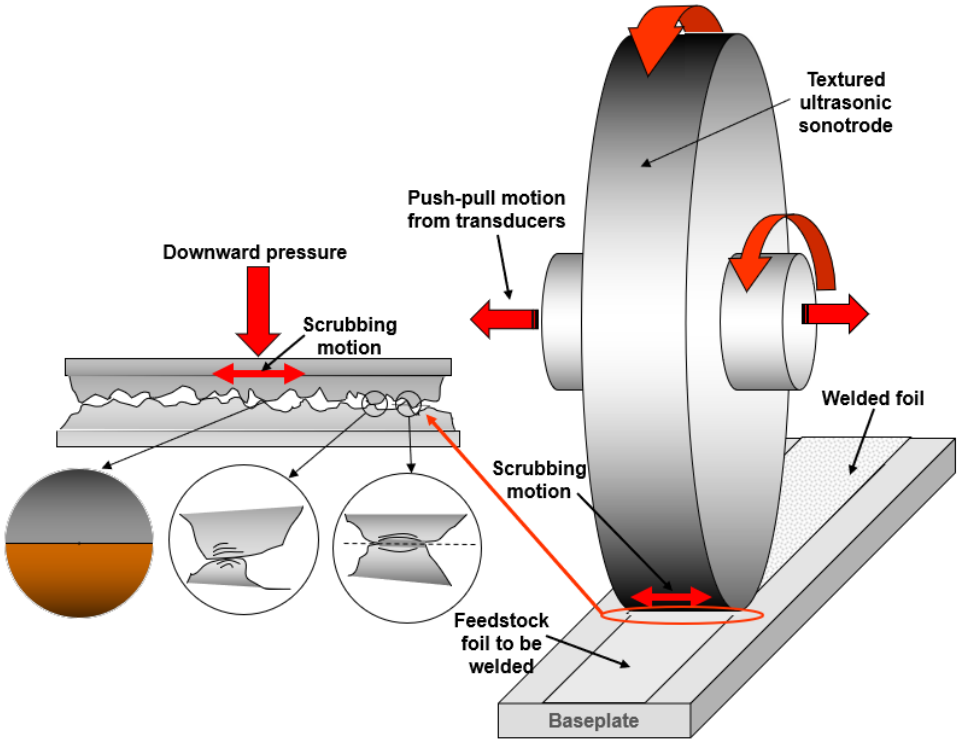


**Figure 1. Illustration of the UAM process. This image was provided courtesy of Fabrisonic, LLC.**

UAM can be used to weld dissimilar metals [11-14] and to embed various materials through the additive and subtractive processes. Previous efforts have demonstrated how ceramic neutron absorbers can be embedded in aluminum alloys for control plate applications in research reactors [15]. The same process can be used to embed sensors within parts fabricated from UAM or near the surface of components manufactured using other processes, as described in the next section.

## 2.2 SENSOR EMBEDDING PROCESS

The sensor embedding process is summarized in Figure 2 for the case of embedding fiber-optic strain sensors. The process is similar when embedding other types of sensors using UAM. First, channels are machined in the baseplate, and the sensors are inserted inside the channels. The channel's width and depth must be carefully controlled to ensure that the sensor is adequately bonded without overstressing the sensor during the embedding process. Next, the UAM process is used to weld additional layers on top of the sensor, thus bonding the sensor inside the deposited layers. Finally, post-machining is performed to remove excess material. Fiber-optics are perhaps the most challenging sensors to embed because of their small size and relative fragility. However, they also may offer the highest potential reward because of their small size, high precision, and their ability to perform spatially distributed measurements of temperature and strain [16-18].

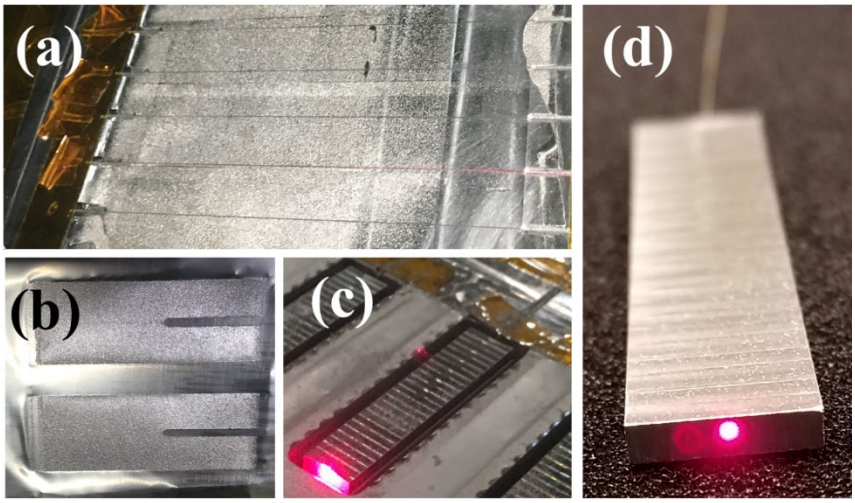


**Figure 2. Sensor embedding process: the sensor is placed inside a machined channel (a), metal foil layers are deposited using UAM (b), and post-machining is performed (c) to deliver a finished part with embedded sensors (d).**

## 2.3 SENSOR SELECTION

Sensor types were selected to best suit the needs of the microreactor community, with a specific focus on HP-based microreactor technologies. The major data gaps for heat pipe–based microreactors are related to thermal and mechanical performance. For example, Los Alamos National Laboratory (LANL) claims that although no comprehensive safety assessment has been performed to date for HP-based reactors, the primary design-basis accident is expected to be related to cascading failure of multiple HPs [19]. In this scenario, a single HP failure would increase the heat that must be rejected from the surrounding HPs in the vicinity of the failure, thus increasing the potential for the surrounding HPs to also fail if thermal limits are exceeded. HP thermal limits are based on (1) sonic velocity limits at the evaporator exit, (2) capillary flow limitations in the wick, (3) entrainment counter-flow limits, and (4) boiling and local dryout near the wall [19]. Therefore, there is a clear need to understand temperature distributions within the HPs and the maximum heat that can be rejected from each individual HP. In addition, the monolithic core block must be able to withstand significant thermal stresses, which have the potential to cause debonding of a HP from the core block and to initiate a cascading failure accident.

Embedded sensors can support the major thermal/structural data needs for the microreactor community if they can provide reliable measurements of temperature and strain distributions within HPs and the core monolith. Temperature distributions can be measured using both thermocouples (TCs) and spatially distributed fiber-optic temperature sensors [16, 17, 20]. Type K TCs were selected because of their availability in small diameter stainless-steel sheaths, which are compatible with the stainless steel materials of the core block and the HPs. The range of Type K TCs also extends beyond the maximum temperatures (~1,000°C) expected during the non-nuclear tests. Fiber-optic temperature sensors can either be loosely held inside embedded stainless steel capillary tubes or in empty channels that can be machined in the part prior to UAM layering (Figure 2a). This loose coupling is required to prevent strain effects from influencing the temperature measurements. On the other hand, spatially distributed strain can be measured by directly embedding metal coated fibers in the component and compensating for temperature effects using loosely-coupled fiber-optic temperature sensors or TCs, similar to previous efforts [2, 3]. Fiber-optic sensors have been demonstrated at temperatures up to 1,000°C [16, 17, 21] and in high radiation environments [22-30]. For extremely high-temperature applications beyond 1,000°C, single-crystal sapphire optical fibers can be used [30-32]. Fiber-optic strain measurements performed during non-nuclear thermal testing could be complemented by obtaining surface measurements using digital image correlation [33, 34].

# 3. RESULTS

## 3.1 TEST ARTICLE DESIGN

The UAM process described above is attractive because it is a low-temperature bonding process that increases the likelihood that the sensors will survive the embedding process. However, to date, the process has primarily been performed on flat components such as plates. The microreactor program requires more complex geometries such as thin-walled HPs and hexagonal core blocks. Embedding sensors within HPs poses two new challenges. First, the round geometry requires special fixtures and slight modifications to the embedding process to allow the UAM layers to bond to the pipe's curved surface. Second, the fixturing also requires internal support of the tube wall to prevent tube deformation due to the applied downforce. Embedding sensors within a miniature hexagonal core block (henceforth referred to as a *mini hex block*) also requires unique fixturing to hold the component while embedding on the flat portions of the component's outer surface. Therefore, this year's efforts focused on adapting the UAM technology to enable embedding of sensors in stainless-steel pipes, as a surrogate for HPs, and hexagonal component geometries. Thick-wall pipes were targeted for this first demonstration to address embedding on curved surfaces before attempting to embed sensors in thinner walled structures. Embedding in thin-walled HPs is being considered for fiscal year 2021, depending on the available budget.

The pipe geometry in which sensors were embedded was chosen somewhat arbitrarily by balancing a reasonably large outer diameter (OD) (76 mm or 3 in.) with what could easily be accommodated in commonly available tube furnaces. The wall thickness (9.5 mm or ⅜ in.) was selected because it is commercially available and thick enough to prevent significant deformation of the pipe during the embedding process. Both the OD and wall thickness are much larger than typical heat pipes, which generally have an OD closer to 16 mm (5/8 in.) and a wall thickness of ~0.7 mm (0.028 in.). A length of 330 mm (13 in.) was chosen to be compatible with the existing infrastructure available at Fabrisonic, LLC. Figure 3 shows the pipe dimensions and configuration of the embedded sensors. TCs were placed 127 mm (5 in.) and 177.8 mm (7 in.) from the end of the pipe. A 101.6 mm (4 in.) length of each fiberoptic strain sensor was embedded in each pipe. An additional 114.3 mm (4.5 in.) termination length was required to prevent significant reflections at the end of the fibers from affecting measurements within the embedded region. The TC and fiber-optic sensor leads were designed to be routed radially outward from the pipes, and threaded holes were also included on each end of the pipe specimens so that the pipes could be attached to flanges for potential flow or vibration testing. The two larger holes on the tops of the pipes were included to secure the pipe to its fixture during the UAM process. Alternate fixturing mechanisms would need to be developed for embedding in HPs.

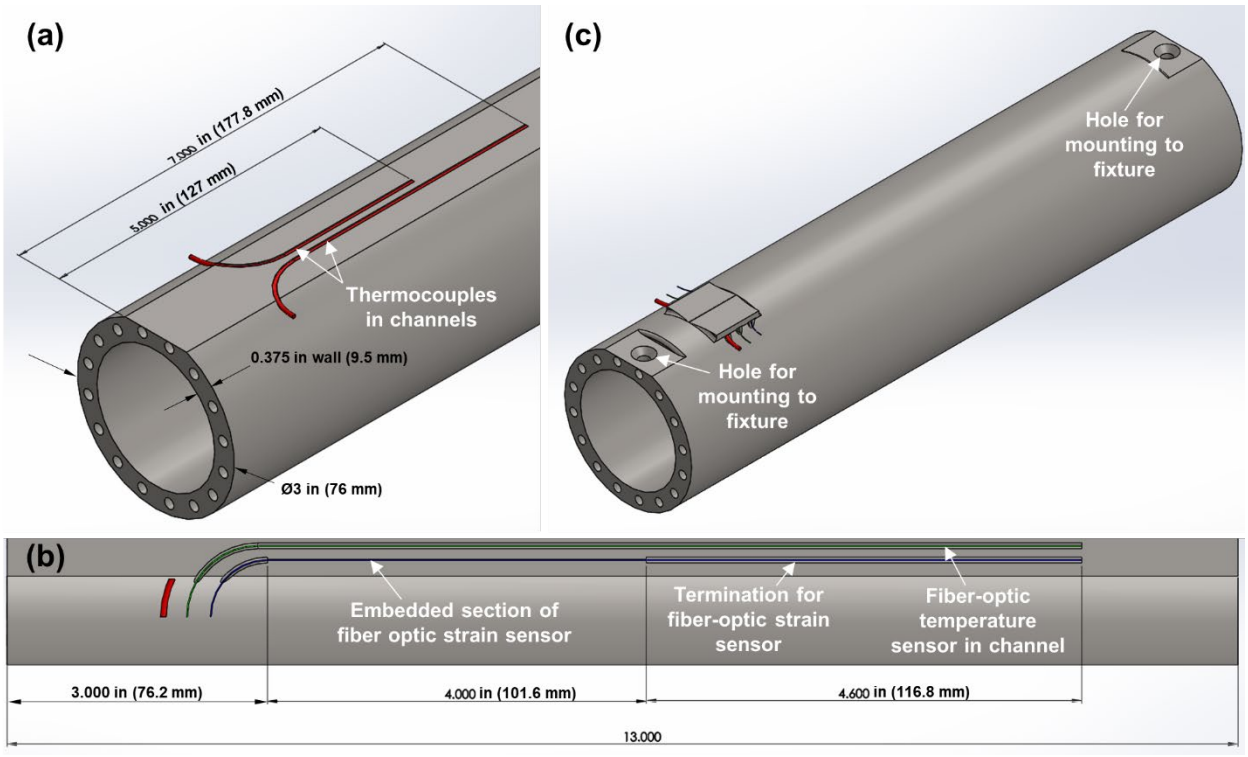


**Figure 3. Geometry of pipe components and placement of embedded sensors showing (a) an isometric view of the channels for TCs, (b) a top-down view of one half of the part showing channels for fiber-optic sensors, and (c) an isometric view of the final design. Note that the fiber-optic sensor channels are hidden in (a).**

The mini hex block was designed and additively manufactured by LANL using a M400-4 laser powder fusion system from Electro-Optical Systems [35]. The 7-hole block was fabricated from 316L stainless steel with post-machining to improve the tolerance and surface finish of the holes and a 900°C vacuum heat treatment to relax residual stresses. Figure 4 shows the mini hex block geometry and the orientation of the embedded sensors. The mini hex block contained two embedded TCs located the same distances from the end of the part as the pipe structures. The fiber-optic temperature and strain sensors also have similar embedded lengths and termination lengths. One notable difference is that the sensors were routed axially along the hex block to be compatible with future single HP testing at INL.

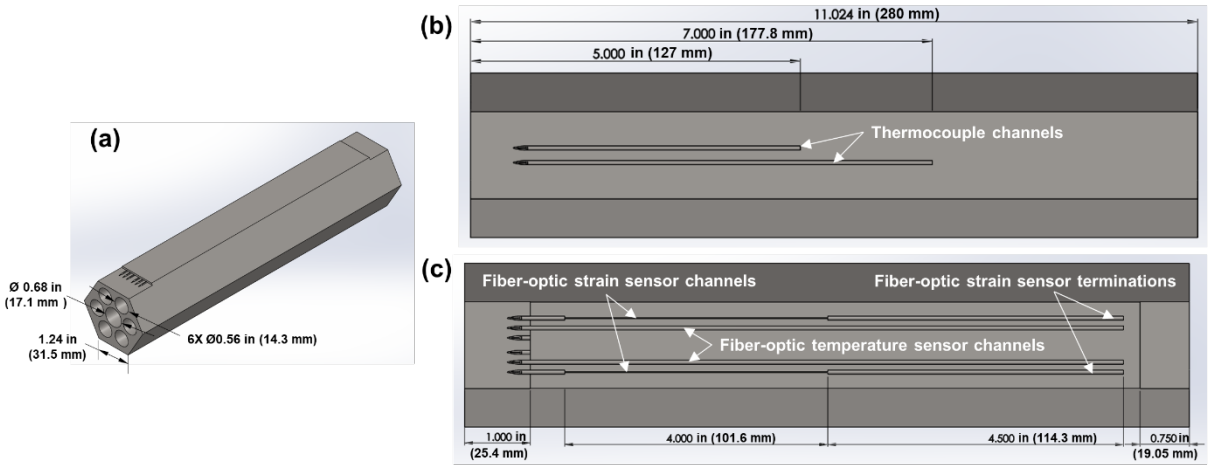


**Figure 4. Geometry of mini hex block and placement of embedded sensors, showing an isometric view of the final design (a), and top-down views of the TC channels (b) and fiber-optic channels (c).**

## 3.2 TEST ARTICLE FABRICATION

Table 1 summarizes the components that were fabricated with embedded sensors, specifying the number of sensors per component, and identifying each embedded fiber-optic strain sensor. One of the embedded strain sensors was broken in pipe 1 (fiber 2) during handling and after embedding, and another strain sensor was broken in the mini hex block during the embedding process (fiber 10).

**Table 1. Stainless steel components with embedded sensors.**

| Component | Embedded fiber-optic strain sensors | Embedded TCs | Cavities for fiber-optic temperature sensors |
|---|---|---|---|
| Pipe 1 | - Fiber 2 (broke)<br>- Fiber 3 | 2 functional TCs per component | 2 per component |
| Pipe 2 | - Fiber 1<br>- Fiber 4 | | |
| Mini hex block | - Fiber 6<br>- Fiber 10 (broke) | | |

Figure 5 shows pictures of the embedding process for the pipe specimens. A special fixture was developed to secure the specimen to a flat steel substrate (Figure 5a). Next, channels were machined with different sizes for the TCs and fiber-optic temperature and strain sensors, and the sensors were placed within their respective channels (Figure 5b). UAM layers were then added to build up the desired thickness (Figure 5c). After finishing UAM (Figure 5d), the excess material was machined to complete the process (Figure 5e). A small cavity is visible in Figure 5d between the leads for the TCs and the fiber-optic strain sensors. Fiber-optic temperature sensors are not currently inserted into these cavities but this step can easily be performed using the open ends of the cavities. This will allow mapping of temperatures during testing and compensation for temperature effects in the fiber-optic strain sensors.

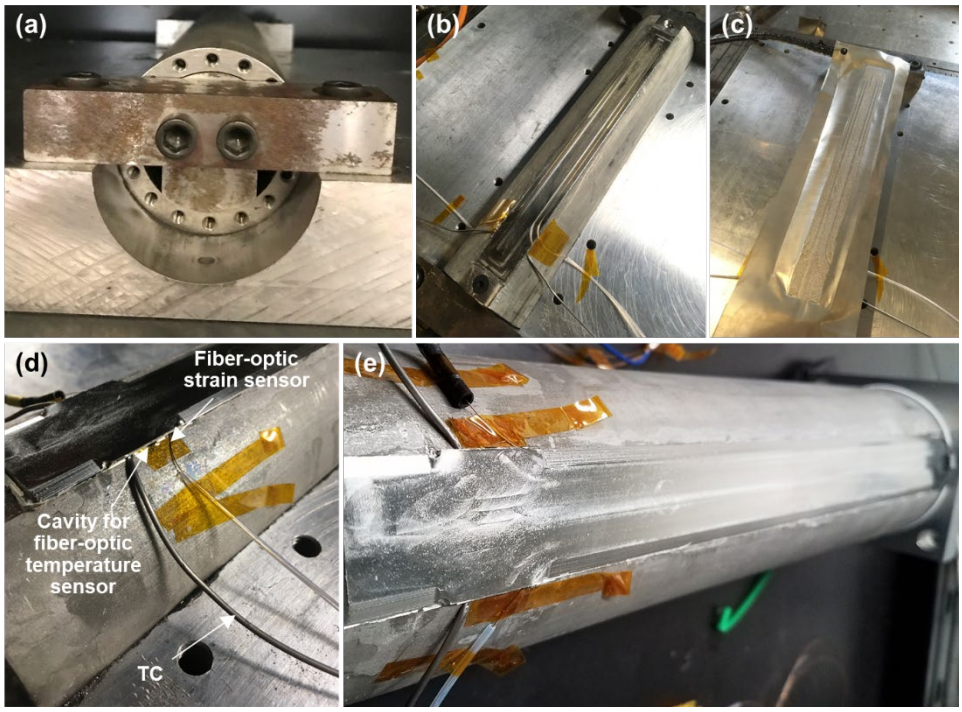


**Figure 5. Pictures of a stainless steel pipe during sensor embedding showing the fixturing setup (a), channel machining and sensor placement (b), UAM layering (c), completion of the UAM layering (d), and the finished part post-machining (e).**

Figure 6 shows pictures of the sensor embedding process for the mini hex block, which was similar to the process for the HP, except that it required a different fixture. Angled mounting brackets were used on either side of the part to secure the part to the baseplate (Figure 6a). Thin shims were placed under the angled mounting brackets to provide fine adjustments. Figure 6b shows the fiber-optic sensors being placed inside the machined channels prior to embedding. Figure 6c shows the UAM layering process, and Figure 6d shows the part after machining. The two ends of the finished part with embedded sensors are shown in Figure 6e and Figure 6f. Note that prior to embedding the sensors the face on which the sensors were to be embedded was machined to reduce its thickness. This ensures that the final part thickness after embedding sensors and adding layers is approximately equal to that of the initial part. Small cavities are visible in Figure 6e between the TC and fiber-optic strain sensor leads. These cavities can accommodate spatially distributed fiber-optic temperature sensors similar to those in the pipe specimens.

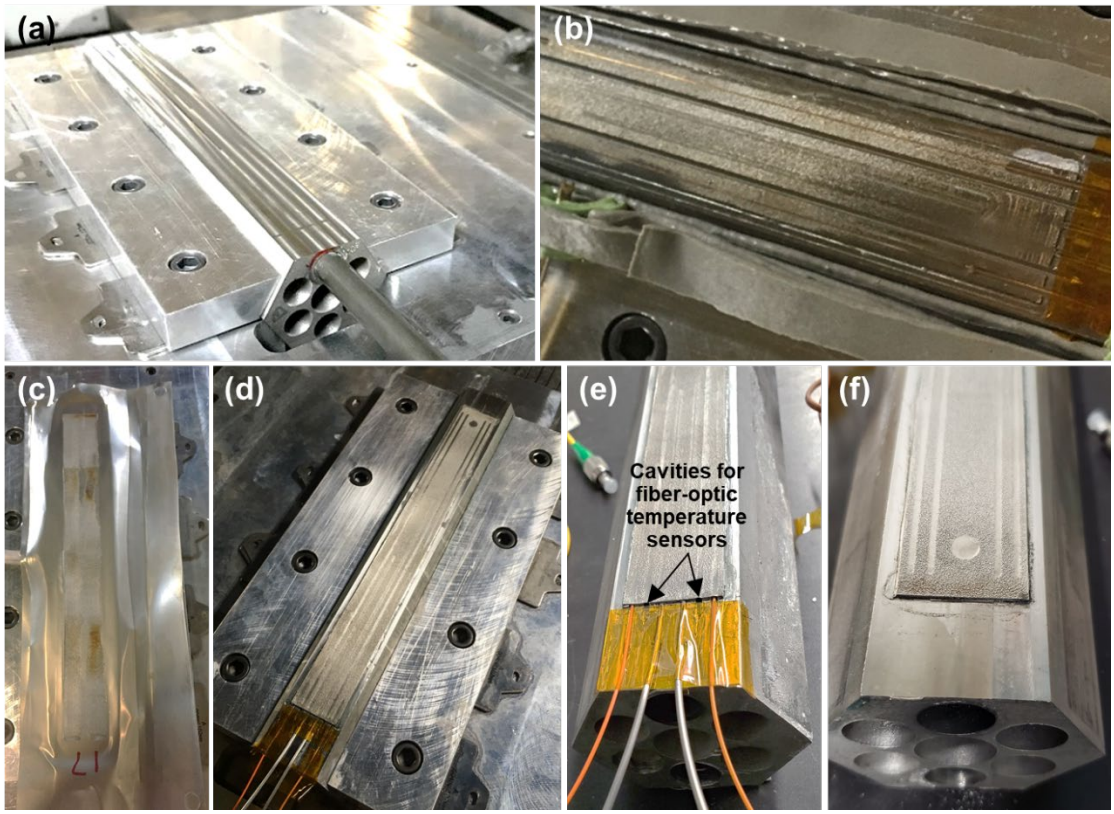


**Figure 6. Pictures of a stainless steel mini hex block during sensor embedding showing the part in its fixture (a), UAM layering (b), completion of the UAM layering process (c), post-embedding machining (d), and the finished part (e).**

### 3.3 SENSOR CHARACTERIZATION AFTER EMBEDDING

The embedded sensors have been characterized for signal attenuation and residual strain to ensure that they survived the UAM process and that they are embedded in the surrounding material. Figure 7 shows residual strain and reflected signal amplitude as a function of position near the embedded region for all fibers that were not broken. Strain data are only shown for which the spectral shift quality (a measure of the strength of the correlation between the pre- and post-embedding scans) is greater than a threshold value of 0.15. This threshold value is discussed in more detail in a previous work [17]. The embedded region is the section that shows significant compressive strain that is generally in the range of 2,000 to 2,500 μm/m, similar to fibers previously embedded in stainless steel plates [3]. The widths of these regions are ~100 mm, which are consistent with the nominal design lengths of the embedded regions shown in Figure 3 and Figure 4. This compressive strain implies that the fibers are well embedded within the stainless steel components, as opposed to the free sections of the fiber that show significantly reduced compressive strain. The slight variations in the strain profiles were likely caused by variations in the channel width or depth during CNC milling. All the sensors generally show no significant reductions in the reflected signal amplitude before, within, and after the embedded region. This is a significant improvement from previous efforts to embed fiber-optic sensors that showed more significant signal attenuation [2]. It is expected that the improvement in signal attenuation is due to the use of a low-bend-loss optical fiber, which reduces microbending losses that can be introduced during the embedding process.

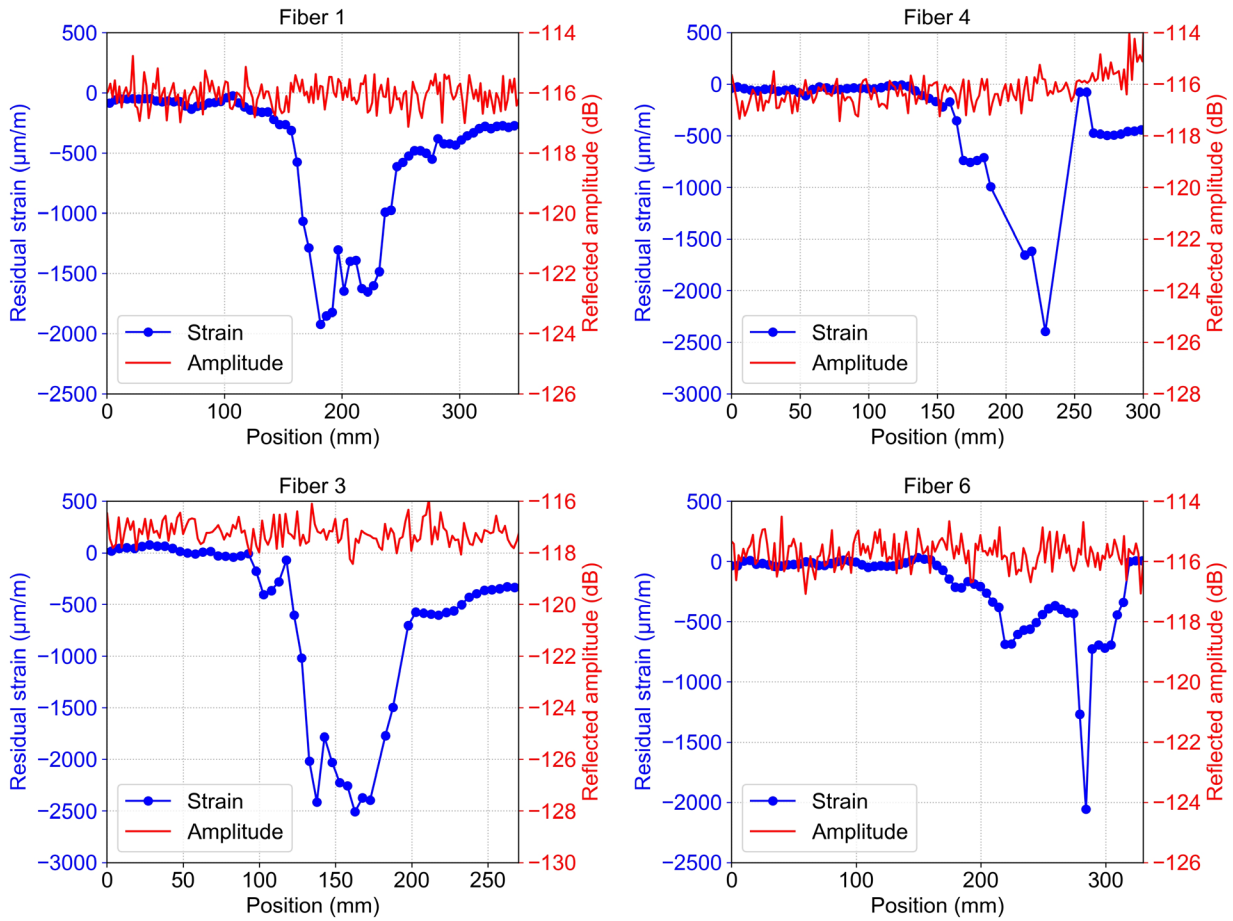


**Figure 7. Reflected fiber-optic signal amplitude and residual strain vs. position after embedding fibers 1 (pipe 2), 4 (pipe 2), 3 (pipe 1), and 6 (mini hex block).**

A simple test was performed to ensure that the fiber-optic strain sensors remain functional after embedding. Strain measurements were taken as a heat gun was used to locally heat a section of pipe 1, starting near the far end of the pipe (x = 200 mm) and moving towards the near end of the pipe (x = 0 mm). Figure 8 shows the measured strain as a function of distance (x) for various times. The measured strain values also include the effects of temperature due to thermo-optic effects and differential thermal expansion between the stainless steel pipe and the glass fiber. Therefore, the strain values as presented in Figure 8 would require temperature compensation similar to that demonstrated in previous efforts [18]. Such compensation is not necessary for this simple demonstration, but it can easily be performed using either the embedded TCs or the cavities that were included to allow insertion of co-located fiber-optic temperature sensors. Nevertheless, the measurements shown in Figure 8 indicate that spatially distributed measurements can be made over a 100 mm length of embedded fiber.

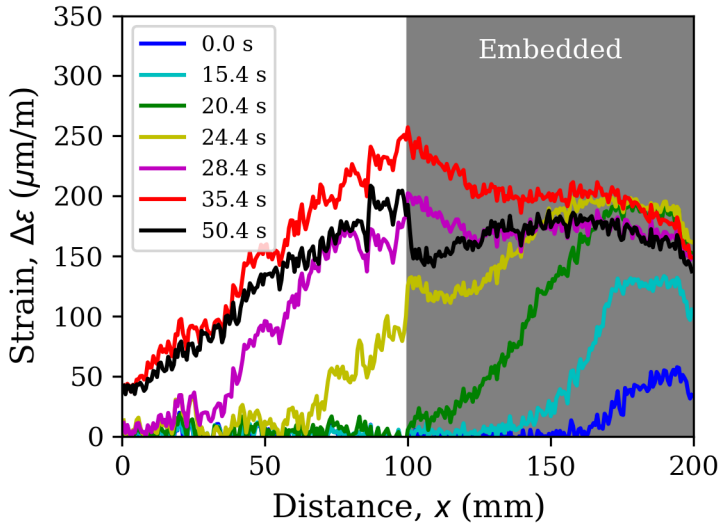


**Figure 8. Spatially distributed strain measured at various times while passing a moving heat source across a pipe specimen with embedded sensors.**

### 3.4 MODELING OF FUTURE EXPERIMENTS

One of the major concerns with any HP-based reactor is that the large monolithic steel structures will have significant temperature gradients which drive thermal stresses. Furthermore, the higher operating temperatures of the core block, the HP's sheath, and the fuel rods' cladding reduce their strength. Higher temperatures also increase fission gas release from the fuel, resulting in higher fuel rod pressurization. Thermomechanical modeling can be used to simulate the temperature distributions and resulting stresses in the monolithic core, the fuel rods, and the HPs due to constrained thermal expansion, as well as rod pressurization. However, these models must be validated through carefully designed experiments. Some of the more uncertain parameters are (1) the strength of the mechanical bond between the fuel and HPs to the core block (if any), and (2) the structures' response to constrained thermal expansion. Other gaps in the current understanding of HP-based reactors are related to the maximum heat that can be rejected from HPs operating at higher temperatures based on limitations on sonic velocity, capillary flow, entrainment counter-flow, and boiling. The results presented in this report demonstrate the feasibility of embedding fiber-optic strain sensors within relevant microreactor components. The next step is to determine whether they can survive and remain bonded to the stainless steel test articles during electrically heated testing to simulate representative thermal stresses in the stainless steel structures. The expected temperatures and strains to which the sensors will be exposed are evaluated later in this Section.

INL is developing the MAGNET facility [36] to allow for electrically heated testing of a large monolithic core block with 37 HPs. If the sensor embedding technology is sufficiently mature, then the sensors embedded in the core block could provide valuable data regarding strain distribution. At the very least, embedded temperature sensors (fiber-optics or TCs) should provide detailed mapping of temperature throughout the core block, which can be used to calculate thermal stresses. A more near-term experiment is being planned to test a single HP inside the center hole of the mini hex block shown in Figure 4 [37]. The remaining six holes will contain cartridge heaters (CHs) to simulate fuel rod heating. The single sodium HP will use a sodium working fluid and will be designed to operate at 650°C. Finite element calculations were performed to estimate the temperatures and thermal stresses to which the embedded sensors might be exposed during testing.

The ANSYS finite element software code package was used to perform 3D steady-state thermal and structural simulations with custom macros developed to model thermal contact conductance between parts separated by insulating gas gaps [38]. The following assumptions were made when modeling the single HP test:

- Dimensions were taken from previous reports for the case with a 152.4 mm (6 in.) long hex block and CHs [37]. Some important dimensions are summarized below:
    - HP: 15.88 mm (0.625 in.) outer diameter (OD) × 14.45 mm (0.569 in.) inner diameter (ID)
    - Center hex block hole diameter: 17.15 mm (0.675 in.)
    - Diameter of 6 holes containing CHs: 14.30 mm (0.563 in.)
    - CH OD: 12.70 mm (0.500 in.).
- The inner surface of the HP was fixed at a constant temperature of 650°C.
- The CHs were modeled as monolithic 304 stainless steel with uniform volumetric heating. The total applied heat load was parametrically varied up to a maximum of 1,902 W (317 W per CH).
- Gas gaps were assumed to be pure helium (He) at 0.75 atm with the following properties:
    - Temperature-dependent thermal conductivity using recommended values for “Helium, He,He(3),He(4)” dataset M1 (1,4) from CINDAS, LLC [39].
- In some cases, boron nitride (BN) paste was assumed to fill the CH-to-hex block gaps and the hex block-to-HP gap. The BN paste was not included in the structural analyses. The following properties were used for the thermal analyses:
    - Temperature-dependent thermal conductivity for “Boron Nitride, BN” dataset M1 (4,2) – C2 from CINDAS.
- The hex block and the HP were modeled as 304 stainless steel (sodium inside the HP was not modeled) with the following properties:
    - Temperature-dependent thermal conductivity using recommended values for “Stainless Steel AISI 304, Fe + Cr + Ni + ..” dataset M1 (8,1) – C4 from CINDAS
    - Temperature-dependent hemispherical total emittance for “Stainless Steels, Fe + Cr + Ni + ..” dataset M1 (3,1) – C2 from CINDAS
    - Temperature-dependent linear thermal expansion for “Stainless Steel AISI 316, Fe + Cr + Ni + ..” dataset M1 (2,1) from CINDAS
    - Temperature-dependent elastic moduli from Table TM-1, Material Group G in Section II, Part D of the 2010 American Society of Mechanical Engineers (ASME) Boiler and Pressure Vessel Code [40]
    - Poisson’s ratio of 0.31.
- 90° rotational symmetry was assumed around the axis of the components.
- Wires that may be wrapped around the HP and/or CHs were neglected.
- Radial and axial heat losses from the hex block were not included.
- Radiation heat transfer was included.
- The structural simulations included temperature-dependent elastic moduli, but only included elastic deformation (no creep or plasticity).

- Stresses are compared with the ultimate tensile stress (UTS) values for type EN 1.4462 stainless steel as a function of temperature [41].

Figure 9 shows an example of the temperature distributions in the hex block and the strain along the face where the fiber-optic sensors are embedded. These results are for the case in which all gaps are filled with helium and the total power is 1,902 W (317 W per CH, 250.2 kW/m$^2$ passed to the HP). Figure 10 shows the resulting stresses in the hex block for the same case. These simulations show that the hex block will see tensile stresses on the inner (colder) surfaces that transition to compressive stresses on the outer (hotter) surfaces due to constrained thermal expansion.

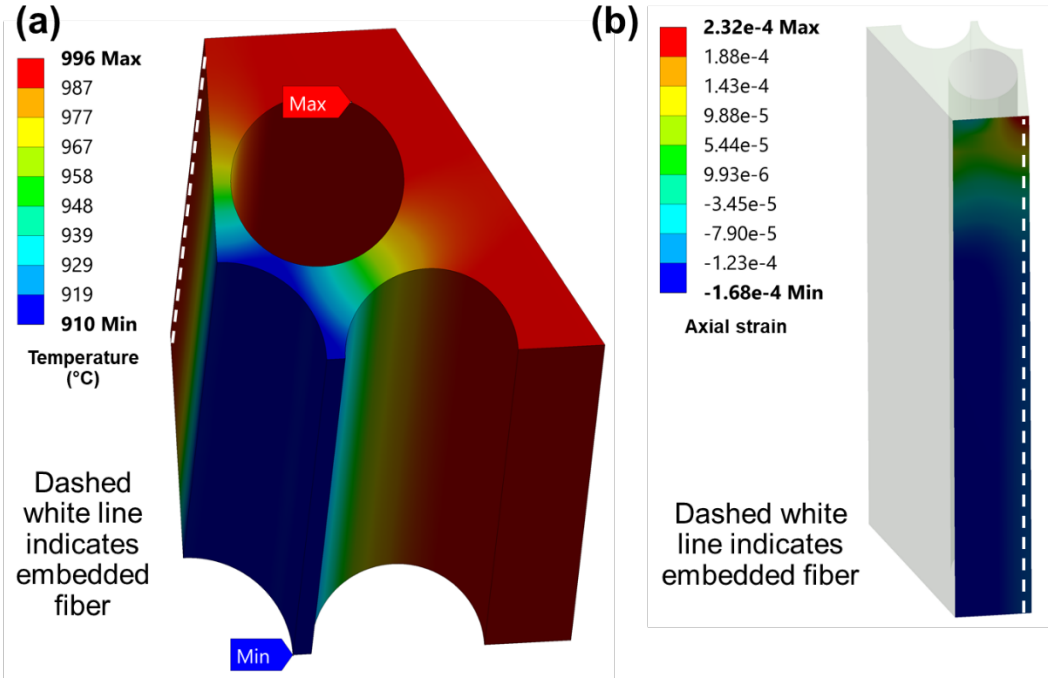


**Figure 9. Calculated hex block temperatures (a) and strains along the face on which sensors are embedded (b) with He-filled gaps and a total power of 1,902 W (250.2 kW/m$^2$ to HP).**

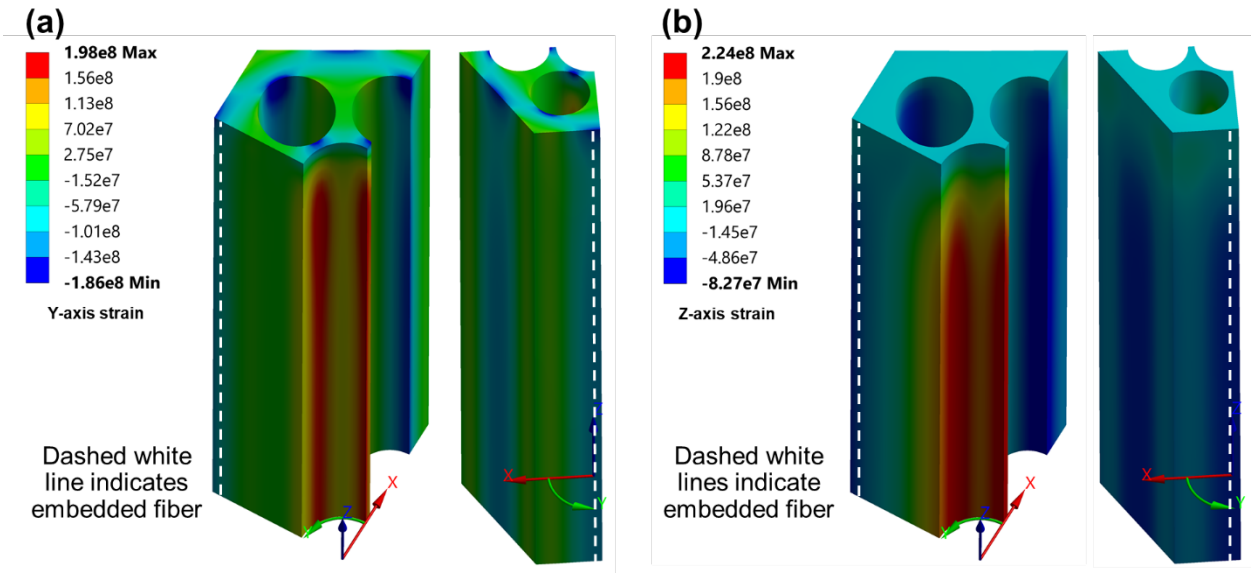


**Figure 10. Calculated Y-axis (a) and Z-axis (b) normal stress distributions in the hex block with He-filled gaps and a total power of 1,902 W (250.2 kW/m$^2$ to HP).**

Figure 11 shows the range of calculated hex block temperatures as a function of heat flux to the HP. Results are shown for various materials filling the gaps surrounding the HP and the CHs. For example, "HP-He, CH-BN" refers to the case in which He surrounds the HP, but the CHs are surrounded by BN. The CHs are limited to a maximum sheath temperature of 760°C. Without surrounding the HP with BN, the CHs can only be operated at a maximum power of ~100 W/CH (79 kW/m$^2$ heat flux to the HP) before the temperature limits of the CH are exceeded, even when the CHs are surrounded by BN. The hex block temperature is most significantly affected by the HP-to-hex block gap. This can be explained based on the heat flux passing between the two gaps. The total heat generated by all six CHs must pass through the gap surrounding the HP, whereas the total heat passing through each gap surrounding the CHs is lower by a factor of 6. Therefore, increasing the thermal conductivity of the gap surrounding the HP would have the most significant impact on the temperature. The temperature gradient through the hex block (determined based on the thickness of the filled region) is not significantly affected by changing the conductivity of the gap surrounding the HP. This only changes the boundary condition at the inner surface of the hex block. However, filling the gap surrounding the CHs with BN greatly reduces the temperature gradients. This is because the more conductive medium allows a larger effective surface area through which the heat generated on the outer side of the CHs can pass before reaching the HP. Without the conductive BN, this heat must pass through the thin wall region between the CHs, which increases the temperature gradients.

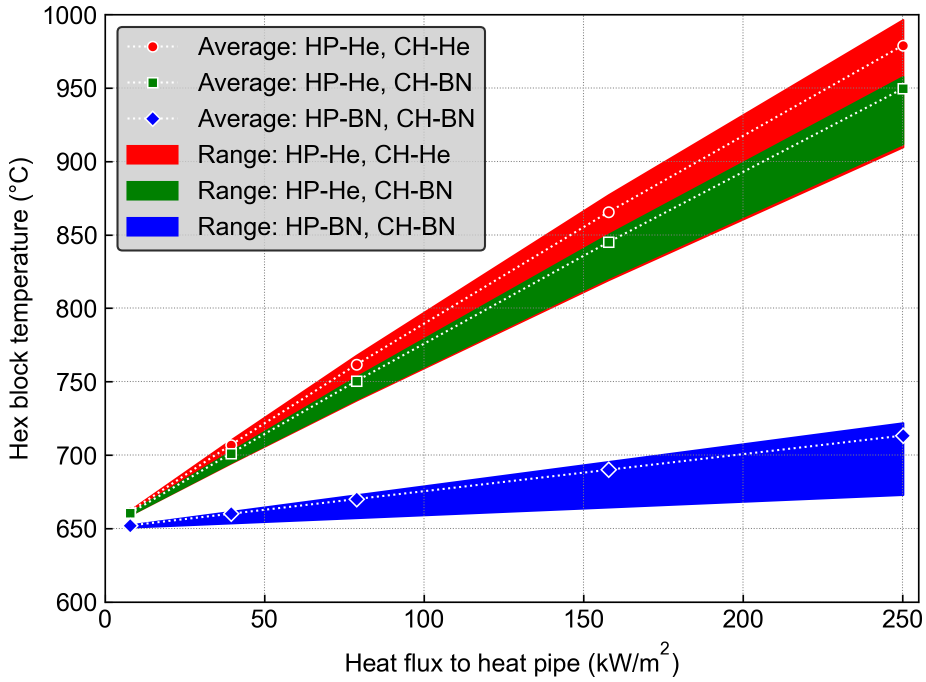


**Figure 11. Hex block temperatures as a function of heat flux to the HP with either He or BN surrounding the HP or CHs, as indicated in the legend.**

Figure 12 shows resulting maximum von Mises stress in the hex block and the UTS (evaluated at the average temperature) as a function of heat flux. As expected, the stress follows the temperature gradient, and the stresses are lowest when the gaps surrounding the CHs are filled with BN. However, the gap surrounding the HP also matters, as the higher temperatures that result from filling this gap with He greatly decrease the UTS of stainless steel. Without surrounding the HP with BN, the structural simulations predict stresses that exceed the UTS of the hex block when the heat flux to the HP reaches values in the range of 160 to 210 kW/m$^2$, depending on whether the CHs are surrounded by He or BN. This is primarily a result of the higher block temperatures (>900°C) when the block is not surrounded by BN and the associated reduction in UTS at the higher temperatures. Immediate failure is not expected to occur for the range of simulated heat fluxes if both gaps are filled with BN.

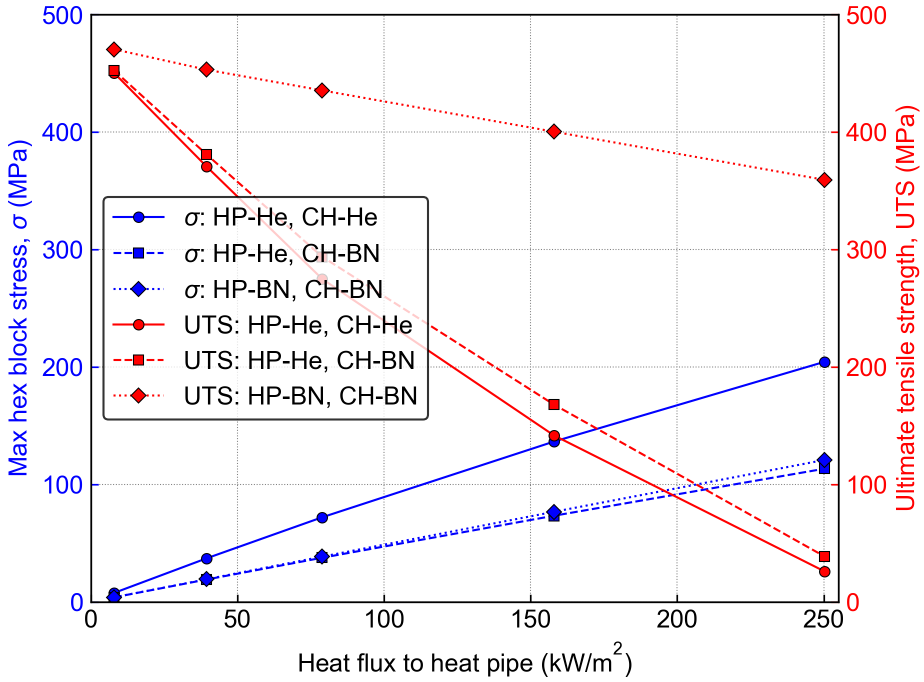


**Figure 12. Maximum von Mises stress and UTS of the hex block with either He or BN surrounding the HP or CHs, as indicated in the legend.**

The sensors are embedded on one of the flat faces of the hex block; an example of the strains calculated throughout that face is shown in Figure 9b, with most of this face in compression. Figure 13 shows the average temperature and Z-axis strain (parallel to the fiber) at the location of the embedded fibers as a function of heat flux to the HP for the same cases shown in Figure 11 and Figure 12. The fiber-optic strain sensors embedded on the outer surface of the hex block would need to measure compressive strains ranging from a few μm/m to as high as 74 μm/m, depending on the gap material and the heat flux. The nominal strain resolution for the fiber-optic sensors is ~1 μm/m. Therefore, strain measurements are possible, but further testing is required to determine whether the embedded fiber-optic sensors can survive the expected temperatures during the experimental testing and the resulting differential thermal strain between the hex block and the fibers. To measure the maximum tensile stresses in the hex block, the fibers must be embedded on the inner surface of the hex block near the HP. However, embedding sensors on the inner surface of a relatively small hole is not possible using UAM, as the sonotrode cannot provide the required ultrasonic scrubbing motion to weld additional layers in such a limited space. Furthermore, noncontact techniques such as digital image correlation also cannot access the inner surface of the single HP experiment. Therefore, the best approach to validating the thermomechanical models of the single HP experiment may be to accurately measure the temperature distributions, calculate thermal stresses, and examine the hex block post-heating to look for signs of failure, plastic strain, or thermal creep. Additional analyses would be required to calculate the expected plastic strains and thermal creep strains.

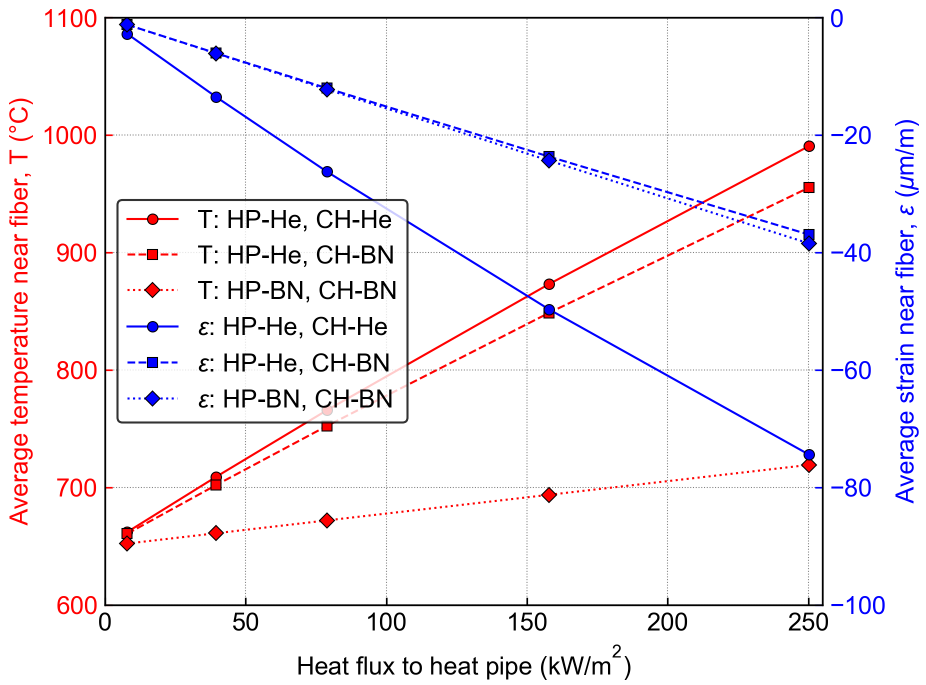


**Figure 13. Average temperature and strain at the location of the embedded fiber vs. heat flux to the HP with either He or BN surrounding the HP or CHs, as indicated in the legend.**

# 5. SUMMARY AND CONCLUSIONS

This report summarizes the initial demonstration of embedding sensors in stainless steel components relevant to HP-based microreactors. TCs and spatially distributed fiber-optic strain sensors were successfully embedded within two pipe specimens and a miniature hex block for future testing in electrically heated, non-nuclear testbed facilities. The sensor embedding process uses UAM to bond stainless steel layers on top of sensors placed inside small machined cavities. The embedded fiber-optic sensors showed minimal signal attenuation and adequate compressive strain after embedding. A simple test was performed with a moving heat source to demonstrate functionality of the embedded sensors. Finite element models were used to simulate the temperatures and stresses to which the embedded sensors would be exposed during testing. Results show that while the embedded sensors may be capable of measuring the relatively small compressive strains near the outer surface of the hex block, the limiting tensile strains occur at the inner surface of the hex block, which cannot be accessed using embedded sensors or noncontact techniques. The simulations also show the importance of using highly conductive materials such as BN to fill the gaps surrounding the HP and the CHs to limit the maximum temperatures, temperature gradients, and the resulting thermal stresses.

## 6. REFERENCES


1. C.M. Petrie et al., *Embedment of sensors in ceramic structures*, ORNL/SPR-2019/1301, Oak Ridge National Laboratory: Oak Ridge, TN (2019).
2. C.M. Petrie et al., "Embedded metallized optical fibers for high temperature applications," *Smart Materials and Structures*, **28** (2019) p. 055012.
3. C.M. Petrie et al., "High-temperature strain monitoring of stainless steel using fiber optics embedded in ultrasonically consolidated nickel layers," *Smart Materials and Structures*, **28** (2019) p. 085041.
4. C. Petrie et al., "Embedded Fiber Optic Sensors for In-Pile Applications," in *11th Nuclear Plant Instrumentation, Control and Human-Machine Interface Technologies* (2019): Orlando, FL, USA, p. 459-468.
5. D.C. Sweeney et al., "Metal-embedded fiber optic sensor packaging and signal demodulation scheme towards high-frequency dynamic measurements in harsh environments," *Sensors and Actuators A: Physical*, **312** (2020) p. 112075.
6. H.P.C. Daniels, "Ultrasonic welding," *Ultrasonics*, **3** (1965) p. 190-196.
7. N. Sridharan and C.M. Petrie, "Ultrasonic Additive Manufacturing," in *Additive Manufacturing Processes*, D.L. Bourell, et al., Eds. 2020, ASM International.
8. N. Sridharan et al., "Rationalization of anisotropic mechanical properties of Al-6061 fabricated using ultrasonic additive manufacturing," *Acta Materialia*, **117** (2016) p. 228–237.
9. M.R. Sriraman, S.S. Babu, and M. Short, "Bonding characteristics during very high power ultrasonic additive manufacturing of copper," *Scripta Materialia*, **62** (2010) p. 560-563.
10. T. Han et al., "Effect of weld power and interfacial temperature on mechanical strength and microstructure of carbon steel 4130 fabricated by ultrasonic additive manufacturing," *Manufacturing Letters*, **25** (2020) p. 64-69.
11. Z.L. Ni and F.X. Ye, "Weldability and mechanical properties of ultrasonic welded aluminum to nickel joints," *Materials Letters*, **185** (2016) p. 204-207.
12. T.H. Kim et al., "Process robustness of single lap ultrasonic welding of thin, dissimilar materials," *CIRP Annals*, **60** (2011) p. 17-20.
13. N. Sridharan et al., "Microstructure and texture evolution in aluminum and commercially pure titanium dissimilar welds fabricated using ultrasonic additive manufacturing," *Scripta Materialia*, **117** (2016) p. 1–5.
14. N. Sridharan, M. Norfolk, and S.S. Babu, "Characterization of Steel-Ta Dissimilar Metal Builds Made Using Very High Power Ultrasonic Additive Manufacturing (VHP-UAM)," *Metallurgical and Materials Transactions A*, **47** (2016) p. 2517-2528.
15. A. Hehr et al., "Five-Axis Ultrasonic Additive Manufacturing for Nuclear Component Manufacture," *JOM*, **69** (2017) p. 485-490.
16. T.W. Wood et al., "Evaluation of the Performance of Distributed Temperature Measurements with Single-Mode Fiber Using Rayleigh Backscatter up to 1000°C," *IEEE Sensors Journal*, **14** (2014) p. 124-128.
17. D.C. Sweeney, A.M. Schrell, and C.M. Petrie, "An Adaptive Reference Scheme to Extend the Functional Range of Optical Backscatter Reflectometry in Extreme Environments," *IEEE Sensors Journal*, (2020) p. 1-1.
18. C.M. Petrie and N. Sridharan, "In situ measurement of phase transformations and residual stress evolution during welding using spatially distributed fiber-optic strain sensors," *Measurement Science and Technology*, **31** (2020) p. 125602.
19. P.R. Mcclure et al., *Design of megawatt power level heat pipe reactors*, LA-UR-15-28840, Los Alamos National Laboratory: Los Alamos, NM (2015).
20. M. Froggatt and J. Moore, "High-spatial-resolution distributed strain measurement in optical fiber with Rayleigh scatter," *Applied Optics*, **37** (1998) p. 1735-1740.

21. A.H. Rose, "Devitrification in annealed optical fiber," *Journal of Lightwave Technology*, **15** (1997) p. 808-814.
22. D.P. Hawn et al., "In-situ gamma radiation induced attenuation in silica optical fibers heated up to 600°C," *Journal of Non-Crystalline Solids*, **379** (2013) p. 192-200.
23. C.M. Petrie et al., "Reactor radiation-induced attenuation in fused silica optical fibers heated up to 1000 °C," *Journal of Non-Crystalline Solids*, **409** (2015) p. 88–94.
24. C.M. Petrie, W. Windl, and T.E. Blue, "In-Situ Reactor Radiation-Induced Attenuation in Sapphire Optical Fibers," *Journal of the American Ceramic Society*, **97** (2014) p. 3883–3889.
25. C.M. Petrie, B. Wilson, and T.E. Blue, "In Situ Gamma Radiation-Induced Attenuation in Sapphire Optical Fibers Heated to 1000°C," *Journal of the American Ceramic Society*, **97** (2014) p. 3150-3156.
26. C.M. Petrie and T.E. Blue, "In situ reactor radiation-induced attenuation in sapphire optical fibers heated up to 1000 °C," *Nuclear Instruments and Methods in Physics Research Section B: Beam Interactions with Materials and Atoms*, **342** (2015) p. 91–97.
27. S. Girard et al., "Radiation Effects on Silica-Based Optical Fibers: Recent Advances and Future Challenges," *IEEE Transactions on Nuclear Science*, **60** (2013) p. 2015-2036.
28. G. Cheymol et al., "High Level Gamma and Neutron Irradiation of Silica Optical Fibers in CEA OSIRIS Nuclear Reactor," *IEEE Transactions on Nuclear Science*, **55** (2008) p. 2252-2258.
29. C.M. Petrie, A. Birri, and T.E. Blue, "High-dose temperature-dependent neutron irradiation effects on the optical transmission and dimensional stability of amorphous fused silica," *Journal of Non-Crystalline Solids*, **525** (2019) p. 119668.
30. C.M. Petrie, *Characterization of the Performance of Sapphire Optical Fiber in Intense Radiation Fields, when Subjected to Very High Temperatures*. 2014, The Ohio State University: Columbus, OH.
31. C.M. Petrie and T.E. Blue, "In Situ Thermally Induced Attenuation in Sapphire Optical Fibers Heated to 1400°C," *Journal of the American Ceramic Society*, **98** (2015) p. 483-489.
32. B.A. Wilson, C.M. Petrie, and T.E. Blue, "High-temperature effects on the light transmission through sapphire optical fiber," *Journal of the American Ceramic Society*, **101** (2018) p. 3452-3459.
33. B.M.B. Grant et al., "High-temperature strain field measurement using digital image correlation," *The Journal of Strain Analysis for Engineering Design*, **44** (2009) p. 263-271.
34. J. Lyons, J. Liu, and M. Sutton, "High-temperature deformation measurements using digital-image correlation," *Experimental mechanics*, **36** (1996) p. 64-70.
35. H.R. Trellue et al., *Microreactor Demonstration and Testing Progress in FY19*, LA-UR-19-28768, Los Alamos National Laboratory: Los Alamos, NM (2019).
36. T.J. Morton, J.E. O'Brien, and J.L. Hartvigsen, *Functional and Operating Requirements for the Microreactor Agile Non-Nuclear Experimental Test Bed (MAGNET)*, INL/EXT-20-58104, Idaho National Laboratory: Idaho Falls, ID (2020).
37. H.R. Trellue et al., *Microreactor Agile Nonnuclear Experimental Testbed Test Plan*, LA-UR-20-20824, Los Alamos National Laboratory: Los Alamos, NM (2020).
38. J.L. McDuffee, "Heat Transfer through Small Moveable Gas Gaps in a Multi-Body System using the ANSYS Finite Element Software," in *Proceedings of ASME 2013 Heat Transfer Summer Conference* (2013): Minneapolis, MN, United States, p. 17783.
39. *CINDAS, LLC: Global Benchmark for Critically Evaluated Materials Properties Data*. 27 July [cited 2016 27 July]; Available from: http://cindasdata.com.
40. *2010 ASME Boiler and Pressure Vessel Code, Section II - Materials (Includes Addenda for 2011)*. 2011, American Society of Mechanical Engineers.
41. J. Chen and B. Young, "Stress–strain curves for stainless steel at elevated temperatures," *Engineering Structures*, **28** (2006) p. 229-239.